Appl. Phys. B 85, 531–538 (2006)
DOI: 10.1007/s00340-006-2415-7

Applied Physics B
Lasers and Optics

M. KOLESIK[1,✉]
E.M. WRIGHT[1]
A. BECKER[2]
J.V. MOLONEY[1]

Simulation of third-harmonic and supercontinuum generation for femtosecond pulses in air

[1] ACMS and Optical Sciences Center, University of Arizona, Tucson, AZ 85721, USA
[2] Max Planck Institute for the Physics of Complex Systems, Dresden, Germany

Received: 21 March 2006
Published online: 31 August 2006 •

ABSTRACT Numerical simulations of third-harmonic and supercontinuum generation for femtosecond pulses propagating in air are presented which, for the first time to the best of our knowledge, do not rely on the decomposition of the total field into slowly-varying fields centered around the fundamental and third-harmonic. The simulation results are interpreted using an effective three-wave mixing approach, and together they provide new insights into the relation between third-harmonic and supercontinuum radiation.

PACS 42.65.Jx; 42.65.Ky; 52.35.Mw

1 Introduction

Third-harmonic (TH) generation obtained using femtosecond pulses in gases has now been studied for more than a decade (see e.g. [1–5]). More recently, understanding the properties of TH generation in air has become even more important [6–9], in a large part due to the promise for remote-sensing applications [10], but also as a potential stable source of high-frequency pulses [11].

The goal of the present paper is twofold. First, we present, for the first time to the best of our knowledge, a self-consistent model including both supercontinuum (SC) and TH radiation effects into simulation of femtosecond pulse propagation in air. In particular, in all previous works a two-envelope approximation has been utilized in simulations of femtosecond pulses in air (see e.g. [6, 12]), one envelope being associated with the SC centered around the fundamental, and the other centered around the TH. This two-envelope approximation can only be justified, and seems to work well [6], in the situation where the spectra of the generated SC and TH signals are well separated. However, TH radiation and supercontinuum can overlap due to extreme spectral broadening, as it was shown for the first time in [13] and demonstrated in an extreme regime in [9]. When super-broadening occurs and the fundamental and TH spectra merge as in [9], the two-envelope approach becomes questionable. Our approach works with the total real optical field, and thus eliminates envelope-based approximations completely. We demonstrate that our model provides results in good agreement with recent femtosecond experiments in air.

Our second goal is to use our simulation results to elucidate the physics that governs TH generation in air using femtosecond pulses, in particular the relation between TH and SC radiation. For this we utilize the simulated far-field spectra, in conjunction with an effective three-wave mixing approach [14], to present an intuitive explanation of the structure and generation mechanism of the SC and TH light. One particularly important conclusion is that these two components can be, in principle, clearly distinguished. Because the angle-integrated experimental spectra "project out" the necessary information to do that, they must be interpreted with extreme caution.

Our simulations were motivated by two recent experiments. In [8], a tight focus geometry was used to find that the third-harmonic radiation is generated in two components, namely a ring, that carries most of the TH energy, and an energetically weaker, axial component (note that a ring structure was also observed in [4], though not exactly in the far field). We present simulation results and discussion for this focusing regime in Sect. 3. The second experiment [9] that influenced our choice of simulated scenarios measured extremely wide dynamical range, broadband spectra obtained in a loose focus geometry. It was shown that the TH and SC components of the spectrum merge as the pulse energy increases, until the TH and SC components can't be distinguished from each other. We study this case numerically in Sect. 4. Section 5 reports comparative simulations aimed at understanding possible interaction and relations between the SC and TH radiation. Finally, Sect. 6 gives a summary and conclusions.

2 Basic model

Our basic model and numerical approach are based on the unidirectional pulse propagation equation (UPPE) [15] in the scalar and radially symmetric approximations, and here we use the so-called z-propagated version [16]. We emphasize that in order to capture generation of the TH radiation no modification is needed in the propagation equation. Rather, the only difference from the "standard" model is that the nonlinear polarization is calculated using the total real electric field, i.e. without resorting to the usual envelope approxima-

✉ Fax: +1 520 621 1510, E-mail: kolesik@acms.arizona.edu

tions in the nonlinear response evaluation. The propagation of the spectral amplitude $\mathcal{E}(z,\omega,k)$ of the optical field along the propagation distance z is governed by the UPPE equation [16]

$$\begin{aligned}\partial_z \mathcal{E}(z,\omega,k) &= \mathrm{i}k_z(\omega,k)\mathcal{E}(z,\omega,k)\\ &\quad+\frac{\mathrm{i}\omega^2}{2\varepsilon_0 c^2 k_z(\omega,k)}\mathcal{P}(z,\omega,k)\\ &\quad-\frac{\omega}{2\varepsilon_0 c^2 k_z(\omega,k)}\mathcal{J}(z,\omega,k)\,,\end{aligned}\tag{1}$$

where

$$k_z(\omega,k)\equiv\sqrt{\omega^2\varepsilon(\omega)/c^2-k^2}\,,\tag{2}$$

is the propagation constant of a plane wave with frequency ω and transverse wavenumber k. The frequency-dependent linear dielectric permittivity $\varepsilon(\omega)$ is taken as real and corresponds to the index of refraction of air parameterized as in [17]. Equation (1) represents a large system of ordinary differential equations, and we use the GNU Scientific Library ODE integrator suite to solve it. Our computational domain has a radius of 5 mm, and its extent in the temporal direction is 800 fs. We use 4096 and 512 sampling points in time and the radial direction, respectively.

An important feature of our model, from the point of view of TH generation, is the nonlinear polarization $\mathcal{P}(z,\omega,k)$. We use temporal Fourier and radial Hankel discrete transforms to obtain the real-space representation of the real field $E(z,r,t)$ from $\mathcal{E}(z,\omega,k)$. Then, the nonlinear polarization due to bound electrons is calculated in the real-space representation as

$$\begin{aligned}P(z,r,t)&=\varepsilon_0\Delta\chi E(z,r,t)\\ &=\frac{\varepsilon_0\chi^{(3)}}{2}\left[E^2(r,t)+\int_0^\infty R(\tau)E^2(r,t-\tau)\,\mathrm{d}\tau\right]\\ &\quad\times E(r,t)\,,\end{aligned}\tag{3}$$

where the memory function of the stimulated Raman effect $R(\tau)$ is parameterized in the same way as in [18]. The nonlinear index of refraction, $n_2=3/(8n)\chi^{(3)}$, was chosen $n_2=2.0\times10^{-23}\,\mathrm{m^2/W}$, such that the critical self-focusing power for a 42 fs pulse is around 10 GW [19], corresponding to ≈ 0.4 mJ. We further assumed that the delayed Raman response and instantaneous electronic Kerr effect contributed equally to the nonlinear optical response, but note that for the pulse duration used in our simulations the contribution of the delayed Raman nonlinear response is small. For comparative purposes, we also switched off the TH generation in some simulations. This is done by replacing $E^2(t)$ in (3) by its time-averaged value, obtained readily as a modulus squared of the complex analytic signal [20], $|A(t)|^2$. If we further normalize the analytic signal to the light intensity, $I(t)=|A(t)|^2$, the formula for the nonlinear polarization then reduces to the usual approximate expression

$$\begin{aligned}P(z,r,t)&=\varepsilon_0\Delta\chi E(z,r,t)\\ &=\varepsilon_0 n_2\left[I(r,t)+\int_0^\infty R(\tau)I(r,t-\tau)\,\mathrm{d}\tau\right]E(r,t)\,.\end{aligned}\tag{4}$$

It is worthwhile to briefly discuss the relation between our approach and the two-envelope method customarily used for capturing TH radiation effects for femtosecond pulses in air. To obtain the two-envelope expression for the nonlinear response [6, 8, 12], one needs to express the field as

$$E^3=\left(\mathrm{Re}\left\{\mathcal{E}_\omega \mathrm{e}^{-\mathrm{i}\omega_0 t}+\mathcal{E}_{3\omega}\mathrm{e}^{-\mathrm{i}3\omega_0 t}\right\}\right)^3$$

where $\mathcal{E}_\omega$ and $\mathcal{E}_{3\omega}$ are the fundamental and TH envelopes. After expanding, and neglecting eight terms with central frequencies corresponding to fifth, seventh, and ninth harmonics, one obtains the expressions for the instantaneous Kerr response of [6]. In a similar way, one can work out the two-envelope expressions for the delayed Raman part of the nonlinear response.

The advantage of our approach over the usual method is two-fold. First, no artificial splitting of the optical field into two slowly-varying envelopes centered around the fundamental and third-harmonic frequencies [6, 8, 12] is needed. Indeed, such splitting is not even unique, though there may be an obvious choice when the TH and SC spectra are well separated and the approach is applicable. However, the splitting leads to pathological propagation when spectral broadening becomes so large that the spectra of both envelopes overlap, in which case a frequency in the overlap region sees a different dispersion for the two envelopes, an impossible situation. The second advantage of our approach is that our spectral solver naturally captures chromatic dispersion of the medium very accurately in an arbitrary wide frequency range. This is important for simulation in regimes in which the TH and SC components of the spectrum overlap.

To proceed we next consider the contribution of free electrons liberated by multi-photon ionization (MPI) to the nonlinear optical response of air. The spectral transform, $\mathcal{J}(z,\omega,k)$, of the current density due to the free electrons is calculated from the real-space current density $j(z,r,t)$ as a function of local pulse time for given z and transverse coordinate r

$$\frac{\mathrm{d}}{\mathrm{d}t}j(t)=\frac{\mathrm{e}^2}{m_\mathrm{e}}\varrho(t,r)E(t)-j(t)/\tau_\mathrm{c}\,,\tag{5}$$

where $\tau_\mathrm{c}=3.5\times10^{-13}\,\mathrm{s}$ represents damping due to collisions, and ϱ is the free-electron density. The evolution of the electron density due to MPI is described by the equation

$$\partial_t\varrho(t)=N_{\mathrm{O}_2}\sigma_{\mathrm{O}_2}I(t)^{K_{\mathrm{O}_2}}+N_{\mathrm{N}_2}\sigma_{\mathrm{N}_2}I(t)^{K_{\mathrm{N}_2}}\,,\tag{6}$$

where due to the short pulse duration we neglect plasma diffusion and recombination, and we also assume relatively weak ionization so that the depletion of neutrals can be also neglected. In the above equation, $N_{\mathrm{O}_2,\mathrm{N}_2}$ denote the number densities of oxygen and nitrogen molecules in air, and the two terms approximate the MPI rates calculated by intense-field many-body S-matrix theory [21] (IMST). The power-laws parameterized by $\sigma_{\mathrm{O}_2,\mathrm{N}_2}$ and $K_{\mathrm{O}_2,\mathrm{N}_2}$ were obtained by fitting the first-principle MPI rates over the interval of intensities 10^{16}–$10^{18}\,\mathrm{Wm^{-2}}$. Specifically, we used $\sigma_{\mathrm{O}_2}=2.72\times10^{-111}$, $K_{\mathrm{O}_2}=6.84$ and $\sigma_{\mathrm{N}_2}=1.62\times10^{-144}$, $K_{\mathrm{N}_2}=8.71$.

The MPI rates we used were calculated for the central wavelength of 800 nm, and we neglected the MPI contribution due to TH radiation. The contribution of the latter is

filtered out from $I(t)$ in (6). The reason for this simplification is two-fold. First, radiation at wavelength far from 800 nm is generally several orders of magnitude weaker than the "fundamental", and despite lower numbers of photons needed to ionize air, the main contribution to MPI generation is still expected to originate at 800 nm. S-matrix calculations show that in the intensity regime of interest (mid of 10^{17} W/m^2) the TH conversion efficiency would have to exceed 1% to cause significant MPI generation by TH radiation. Second, adding separate contributions to MPI corresponding to fundamental and TH radiation only makes sense when their spectra do not overlap. In most cases, as discussed below, this is not the case.

3 Tight focusing geometry

In the next two sections we present simulation results from our numerical studies motivated by the recent experimental results of Théberge et al. [8, 9]. We choose the pulse duration (FWHM) as 42 fs, similar to that in the experiments, and vary the total pulse energy. The initial Gaussian beam was focused in air to create a filament and generate TH and SC spectra. In order to make the simulations more manageable, we first propagate the pulse linearly one half of the linear focal distance, thereby making it possible to use a smaller simulation domain, then we propagate the pulse beyond the focus in the full, nonlinear regime, until the spectral power spectrum stabilizes. For our first example, motivated by [8], the focus of the incident beam is chosen quite tight, with a focal distance of $f = 50$ cm. The Gaussian beam waist on the lens was 0.25 cm. Thus, compared to the experimental conditions of [8], both the focal length and beam waist are smaller by a factor of two, resulting in a similar focusing geometry. We note that effects of varying the focal length in the tight focus regime was studied in some detail in [22].

Figure 1 shows the far-field intensity profiles of the TH portion of the spectrum, obtained by spectrally filtering the field after propagation, for several pulse energies. The simulated behavior reproduces the experimental and simulation results of [8] very well. The TH far field exhibits a distinct ring structure in addition to an axial or on-axis component. The rings correspond to the angle of propagation of about 6 mrad. While at lower energies the ring intensity grows faster than the on-axis intensity, at higher energies the axial TH radiation catches up and the on-axis intensity of TH radiation becomes comparable with that of the ring. However, the energy carried by rings is significantly higher than that of the axial TH, even at high pulse energies. This is illustrated more quantitatively in Fig. 2 which shows the axial and ring TH energies as a function of input energy, and is analogous to Fig. 4 in [8]. The overall behavior is similar to the experimental observation, and the TH energy is captured quite accurately at higher pulse energies. The main difference between simulation and experiment is the absence of the sharp crossover in the total TH energy seen in the experiment around the critical pulse energy of ≈ 0.4 mJ (a similar kink was observed also in [3]). Instead, the simulated cross-over is rather gradual, and this feature is also present in the simulations based on the two-envelope approximation.

We would like to note that while the integrated quantities such as the energy of the ring and axial components of the TH radiation are quite robust with respect to details of the model, small-scale features of the TH spectral power as a function of angle and frequency are somewhat model and parameter dependent. For example when we lumped the plasma response into the polarization instead of current, as it is sometimes done [16], we have seen changes in the details of the TH region of the far-field spectrum although the global picture remained unchanged.

It is illustrative to examine the spectrally resolved far field of the complete transmitted field with no spectral filtering. An example of this is shown in Fig. 3 which shows a map of the logarithmic spectral power as a function of angular frequency and transverse wave-number. This figure illustrates the key point that in the tight focus geometry the TH component remains well separated throughout the propagation from the SC generation that grows around the fundamental frequency, even for the largest input energy. In this regime, practically all energy in the TH frequency region is due to TH generation, while contribution of supercontinuum to very high frequencies is small (cf. [22]). The clean separation of the TH and SC spectral components explains why our results obtained without envelope approximations agree so well with those obtained using the two-envelope approximation [8].

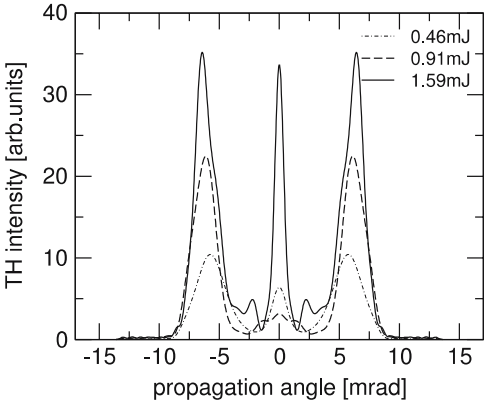

FIGURE 1 Third-harmonic rings observed in the spectrally filtered far-field spectra of femtosecond pulses tightly focused in air. The vertical scale preserves the relative intensities between different pulse energies, but is otherwise arbitrary

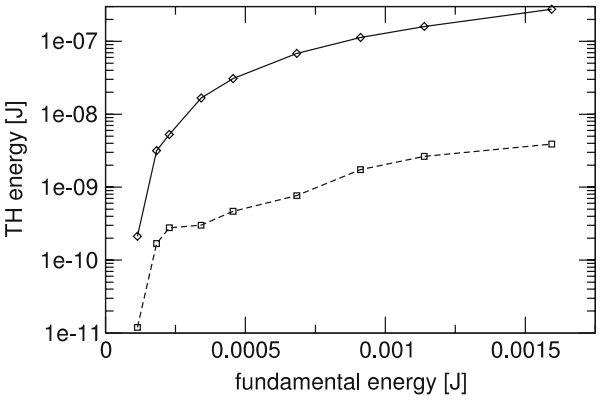

FIGURE 2 Energy of the ring (*diamonds*) and axial (*squares*) components of the third-harmonic radiation as a function of the input pulse energy

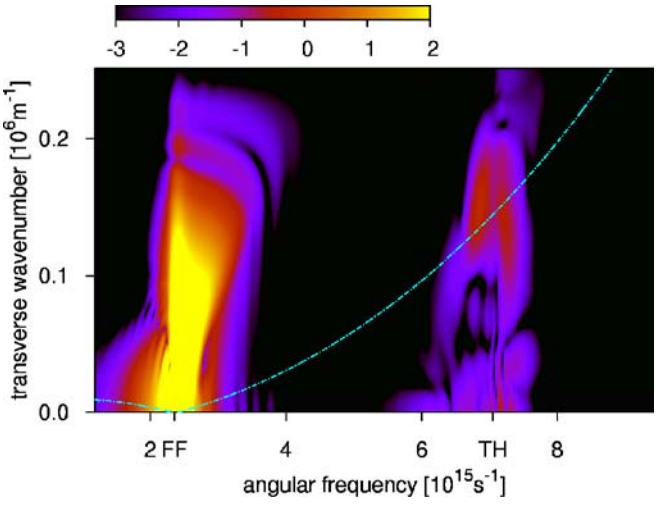

FIGURE 3 Logarithmic far-field spectral power of a 1.14 mJ pulse. Both the fundamental spectral component (*left*) and the third-harmonic (*right*) show modest broadening, but remain well separated. The third-harmonic radiation spectrum exhibits a weaker maximum on-axis (*bottom right*), while most of its energy is concentrated in the ring structure (*upper right*). The *blue line* marks the locus of phase-matching between the fundamental and waves scattered off the medium's nonlinear response. In this and similar pictures, we choose to over-saturate the most intense parts of the spectrum to make the low intensity structure more visible

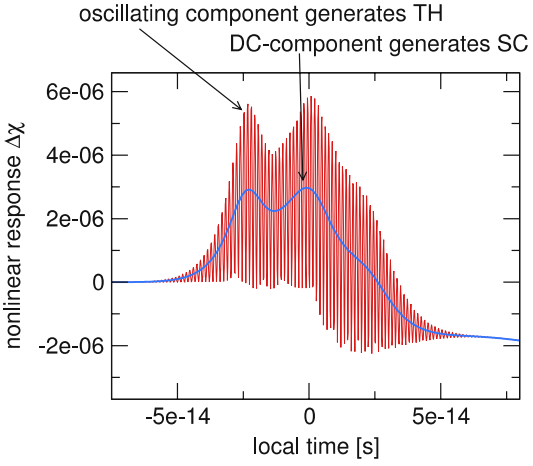

FIGURE 4 An example of the on-axis nonlinear response for an ultrashort pulse propagating in air. The nonlinear susceptibility modification is due to the combination of the Kerr effect and plasma defocusing. It exhibits an oscillating component at roughly the second harmonic of the fundamental. It is the oscillating or "ac" components that gives rise to the third-harmonic radiation. The slowly varying "dc" component generates the super-continuum spectrum

To intuit the structure of the far-field spectrum, we employ the effective three-wave mixing argument used previously for analysis of X-waves and SC in nonlinear dispersive media [14, 23, 24]. The three-wave mixing picture is based on the notion that the femtosecond pulse spectrum can be viewed, at least qualitatively, as a result of scattering of the incident fundamental carrier wave off the "scattering potential" due to the nonlinear response $\Delta\chi$ of the medium. In that spirit, one approximates the polarization by $\Delta\chi(z,t,r)\exp(\mathrm{i}k_z(\omega_0,0)z - \mathrm{i}\omega_0 t)$ and formally integrates the propagation equation (1) to obtain

$$\mathcal{E}(z,\omega,k) \approx \int_{-\infty}^{z} \mathrm{d}z\,\Delta\chi(z,\omega-\omega_0,k)\mathrm{e}^{-\mathrm{i}\Delta K(\omega,k,\omega_0)z}$$

$$\Delta K(\omega,k,\omega_0) = k_z(\omega,k) - k_z(\omega_0,0) - (\omega-\omega_0)/v\,. \qquad (7)$$

Here, we have transformed into a frame moving with the velocity v chosen such that the spatio-temporal spectrum of the nonlinear optical response $\Delta\chi(z,\omega-\omega_0,k)$ varies slowly with z. This equation shows that the loci where the energy concentrates in the (ω,k) plane will depend on the interplay between two factors. First, setting the fast oscillating exponent in (7) to zero determines a phase-matching condition. Second, the power spectrum of the nonlinear perturbation $\Delta\chi(z,\omega-\omega_0,k)$ determines the extent to which the phase-matched processes will be seeded, or driven by the propagating field.

An example of the on-axis ($r=0$) profile of the nonlinear response is illustrated in Fig. 4. It shows that the response exhibits a slowly varying or "dc" component, and a fast oscillating or "ac"component with the frequency around the second harmonic. The velocity v that enters the phase-matching condition is slightly different for different maxima of the dc component [14]. By examining the raw numerical data we can extract the velocities v for the peaks in the nonlinear optical response, and then setting $\Delta K(\omega,k,\omega_0)=0$ in (7) we are able to find the phase-matching condition in the (ω,k) plane. On the other hand, for the oscillating part of the response, the appropriate velocity is equal to the phase velocity of the fundamental, $v=v_0=c/n(\omega_0)$. Note that at $\omega=3\omega_0$ the phase matching condition $\Delta K(3\omega_0,k,\omega_0)=0$ reduces to the standard four-wave mixing condition used in [8].

In Fig. 3, the corresponding phase-matching condition (for $v=v_0$) is shown as the blue line. Let us first consider the origin of the on-axis TH component. Because the oscillation of the response is given by the second harmonic of the fundamental, $|\Delta\chi(z,\omega-\omega_0,k)|$ will exhibit a local maximum at $\omega-\omega_0\approx 2\omega_0$, $k=0$. This is the driving "source" of the on-axis TH radiation. Since $\Delta K(\omega,k=0,\omega_0)\neq 0$, the on-axis TH radiation is not phase-matched, but it has a strong driving source due to the fundamental input . As a consequence, the on-axis TH radiation appears to be locked with the fundamental that drives it [6, 8, 13], and the two components propagate together.

To understand the occurrence of the TH ring, one needs to note that $|\Delta\chi(z,2\omega_0,k)|$ decreases as the transverse wavenumber k grows. Consequently, the TH intensity decreases with the angle of propagation. However, for a sufficiently large angle when $k^2\approx 2k_z(3\omega_0)(k_z(3\omega_0)-3k_z(\omega_0))$, the phase matching occurs at the TH frequency, i.e. $\Delta K\approx 0$. The seed for the TH ring is relatively small as the fundamental dominantly drives the axial TH field, but the weak seed for the TH ring is offset by the fact that it is phase-matched and can grow, and TH radiation is again generated efficiently giving rise to the characteristic ring structure in the spectrum. The angular thickness of the ring reflects the "accuracy" of the phase-matching which is controlled by the effective interaction length that contributes to the integral in (7). This effective interaction length is in turn controlled by the input focusing conditions, and is relatively short for the tight focusing con-

ditions considered in this section. From the above discussion it follows that spatially narrow structures in the nonlinear response $\Delta\chi$ will favor the TH ring, while broader structures emphasize the axial part of TH radiation.

4 Loose focusing geometry

For our second example, motivated by the experiment reported in [9], the linear focal distance is chosen as $f = 200\,\text{cm}$, and the beam waist as 0.25 cm. This choice is meant to reflect the loose focusing used in the experiment.

In this weaker focus geometry a longer filament is created, and the longer effective interaction length results in an explosive spectral broadening of the fundamental spectral component, eventually giving rise to an extremely wide SC spectrum. For low pulse energy, when the SC spectral broadening is moderate, the TH spectrum is well resolved from the SC, and exhibits a multi-peaked structure as shown for an energy of 0.46 mJ in Fig. 5. This figure shows the logarithm of the angle-integrated spectrum for the propagating field versus wavelength for several pulse energies. As the pulse energy increases, the SC spectrum extends into the TH spectral region, and eventually TH and SC spectra completely merge. This behavior was observed in the experiment of [9], and is well reproduced in our simulations as is illustrated in Fig. 5.

The qualitative agreement between experiment and our simulation is very good. However, in the simulation the TH-SC merging occurs at lower pulse energies. While uncertainty in the model parameters most likely contributes to this, we speculate that also the way the spectra are measured in the experiment affect the energy at which the crossover between separated and merged spectra appears to occur. Namely, the experimental spectra do not collect all the light, but partially suppress the off-axis portion of the beam. This may shift the observed merging towards higher pulse energies by damping the contribution of SC propagating at large angles.

In Fig. 6 we compare the far-field spectra for three pulse energies. The first is for 0.51 mJ and corresponds to the second panel in the previous figure. Here, the SC and TH spectral components are still well separated, but it can be seen that the SC radiation grows into the high-frequency region. The second panel in Fig. 6 is for an energy of 0.57 mJ. While in the angle-integrated spectrum shown Fig. 5 the TH peak is barely visible against the broad background, the far-field spectrum clearly shows that TH and SC spectral components remain separated in the transverse wavevector. This is also the case for the spectrum at 0.8 mJ shown in the bottom panel where the high-frequency SC extends well beyond the TH region. Thus, despite their apparent merging in the integrated spectra in Fig. 5, the third-harmonic and supercontinuum processes can still be well resolved in their far field spectra.

Another feature worth noting is the TH rings. Unlike in the tight focus case, the TH rings are much weaker for the loose focus, and most of the TH radiation propagates along the axis. This can be easily understood in terms of the mechanism described in the previous section. First, longer interaction distances result in the stricter phase matching requirement for the ring, which in turn is manifest in an angularly narrow ring. Second, a loose focus creates nonlinear response structures that are spatially wider and their spatial spectra correspondingly narrower. Consequently, the "scattering potential" that gives rise to the ring is also weaker and the ring becomes less pronounced. The same tendency, namely narrower cone of propagation is also evident in the far field spectrum as a whole (compare Figs. 3 and 6).

To conclude this Section we note that the angular distribution of the super-continuum radiation, can also be explained

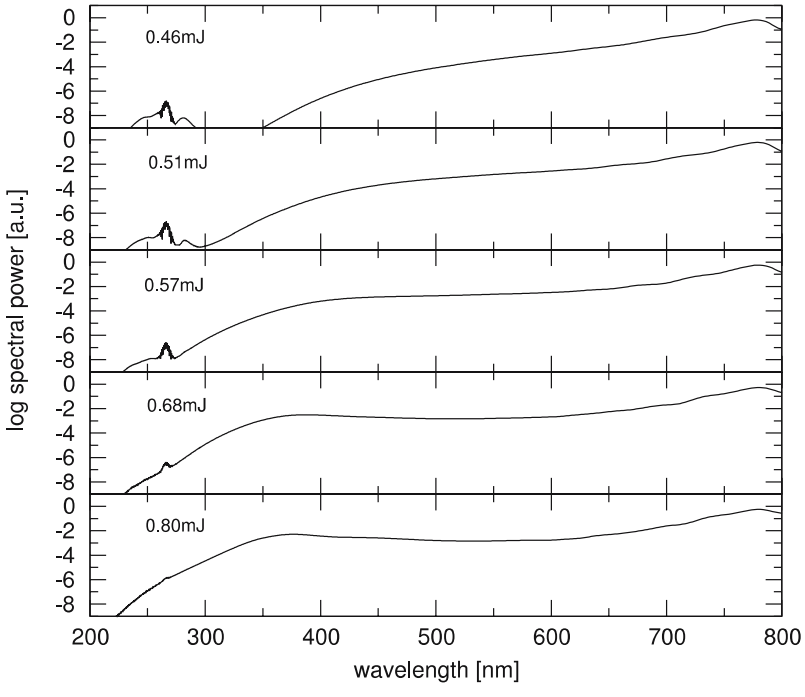

FIGURE 5 Angle-integrated spectra of weakly focused 42 fs pulses in air for several pulse energies

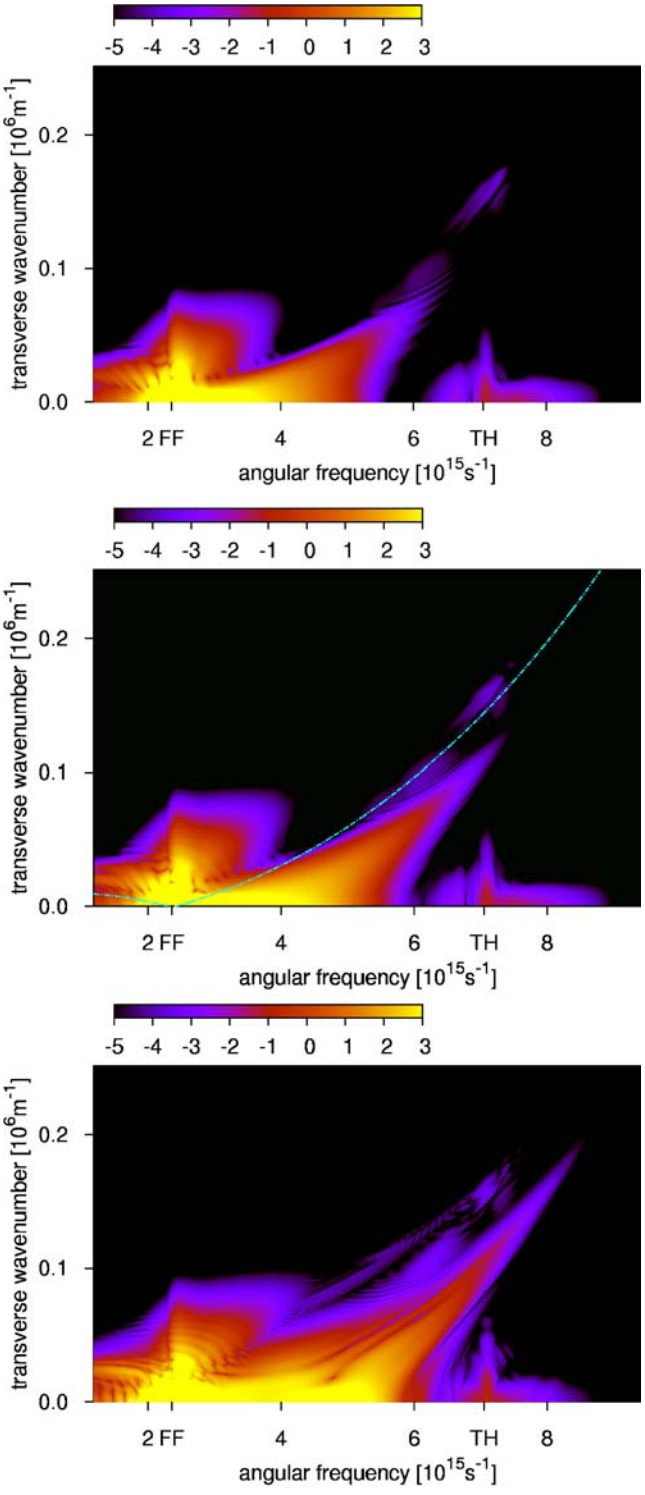

FIGURE 6 Far-field spectra for the loose-focus geometry and pulse energies of 0.51 mJ, 0.57 mJ, and 0.8 mJ (*top* to *bottom*). TH and SC spectral components remain directionally separated as the SC component expands into the high-frequency region. Note that, compared to tight focus, the TH ring structures are weaker but are located tighter along the locus of phase-matched generation shown as a blue line in the middle panel

using the three-wave mixing argument [23]. In particular, the long, high-frequency "arm" of the super-continuum spectrum seen in far-field spectra figures can be related to the nonlinear response "pulses" the same way as in [14].

5 Modification of SC by TH generation

In this section we approach the question of whether the generated TH can modify pulse propagation in air: if we remove the TH field will the pulse propagate largely unchanged? It was recently suggested [12, 25] that the generated TH radiation actually induces the growth of the SC spectrum into the extreme high-frequency region, and is responsible for the spectral energy in the region between 200 and 500 nm.

In order to assess how much influence the TH radiation exerts on the rest of the ultrashort pulse, we performed comparative simulations. Namely, we have switched off the TH generation in the nonlinear response as described in Sect. 2, and performed the simulation for the exactly same conditions of our numerical experiment as with the full model. Figure 7 shows a comparison of the far-field spectra obtained for a 0.68 mJ pulse in the loose focus geometry with and without TH effects included in the model. Clearly, apart from the TH component of the spectrum disappearing in the reduced model, there is almost no change in the rest of the spectrum. This shows that the mechanism of the SC generation doesn't change in the presence of the TH radiation,

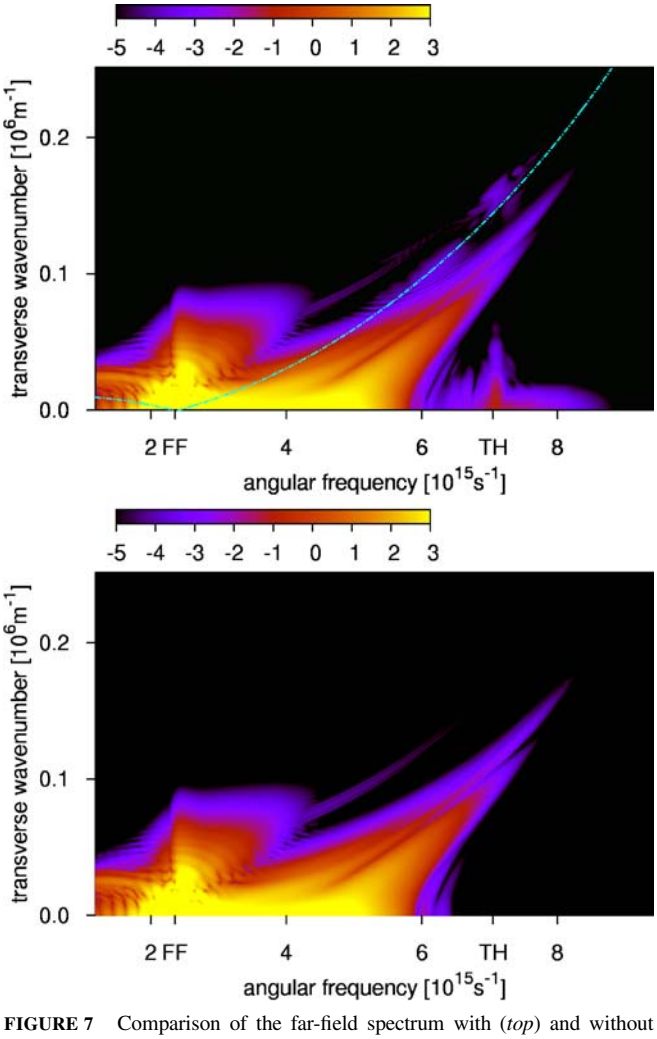

FIGURE 7 Comparison of the far-field spectrum with (*top*) and without (*bottom*) TH generation included in the model. Apart from the TH radiation itself, there are only minimal changes in the rest of the spectrum.

and that the TH contribution to the SC spectral broadening is small.

The robustness of the SC spectrum with respect to the presence or absence of the TH radiation strongly suggests that the interaction between TH and the rest of the pulse is almost a "one-way" process: The radiation around the fundamental frequency, being the most energetic part of the pulse, strongly drives the TH radiation, but the effect of the TH radiation on the fundamental, and on the SC generation is weak compared to other nonlinear processes. Of course, the above conclusion doesn't imply that the TH radiation can be neglected. Because we deal with a highly nonlinear system, even minute perturbations caused by the TH radiation can grow significantly if the effective interaction length is sufficiently long. To illustrate this, we performed another set of comparative simulations in a collimated geometry. In order to increase the length of the filament, we also increased the pulse duration to 120 fs (we also increased the temporal size of our computational domain to 1600 fs, and the number of grid points to 8196), and pulse energy to 6.25 mJ.

Figure 8 shows the linear plasma density with and without TH generation included in the model. As expected, and in accordance with simulations of [12], there is a similarity between the two plasma generation curves immediately after the filamentation onset. Later, the two curves deviate from each other more and more, until the similarity is almost completely lost. The gradual loss of correlation (with increasing propagation distance) between our comparative runs is manifest also in the far-field spectra shown in Fig. 9 in which the details of the spectra appear uncorrelated. However, the global structure and the extent of the spectra are still very similar.

Thus, for a sufficiently long interaction distance (filament length) the presence of the TH radiation eventually causes the pulse evolution to deviate completely from that without TH. This deviation, however, is simply a result of the sensitivity of the system to small "perturbations" caused by the TH radiation in very much the same way a chaotic system is sensitive to small changes in initial conditions. It by no means indicates that the underlying processes are qualitatively different because of the presence of the TH radiation.

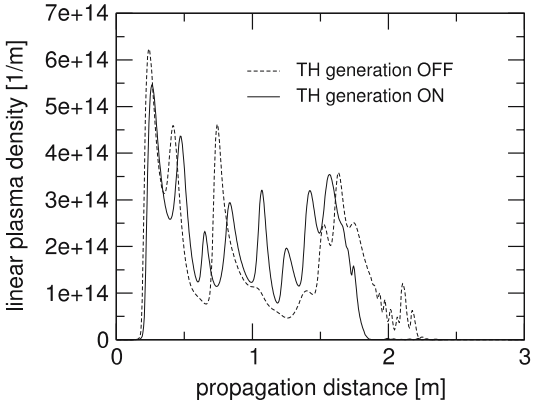

FIGURE 8 Linear density of generated electrons in a collimated femtosecond pulse with and without inclusion of the TH radiation. Correlation between the pulse evolutions decreases with the propagation distance

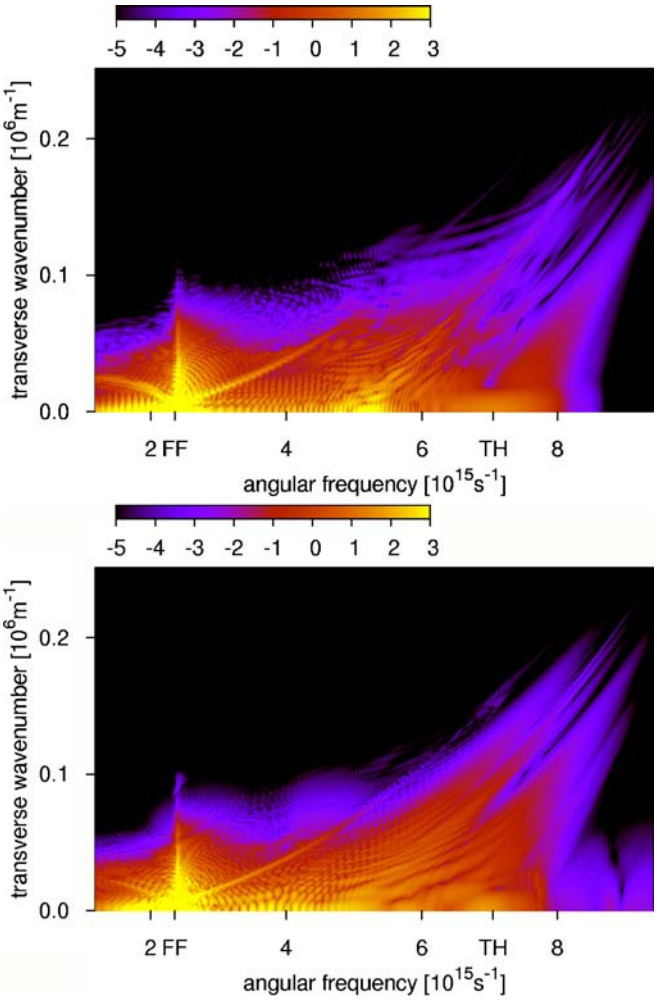

FIGURE 9 Far-field spectrum with (*bottom*) and without (*top*) TH generation included in the model. Different small-scale features indicate that the resulting pulse wave-forms are affected by the presence of TH radiation. Similarity in the global structure of the spectra indicates that the underlying physical mechanism controlling SC generation does not depend on TH generation

6 Summary and conclusions

Numerical simulations based on a unidirectional pulse propagation equation have been shown to agree well with experimental observations of third-harmonic radiation properties in air. This model, though numerically more expensive than a two-envelope approach, offers a physically self-consistent description free of the ambiguity of splitting the physical field into two envelope components. The two-envelope approximation can work well if the spectra of both envelopes remain narrow, the experiment-theory comparison in [8] being a nice example of this. However, in a weak focus geometry, supercontinuum and third-harmonic spectra overlap on the frequency axis. Then the decomposition into two envelopes becomes more problematic, especially when simplified models are used to describe chromatic dispersion around fundamental and third-harmonic frequencies.

We have utilized simulated far-field spectra in three different regimes to obtain new insights into the spectral dynamics

of fs pulses generating third-harmonic radiation in air. Using the effective three-wave mixing picture, we argue that both the third-harmonic and super-continuum components of the spectrum can be qualitatively understood as generated by "scattering" of the fundamental carrier off the local perturbations of the medium susceptibility. While the super-continuum radiation is generated by the slow (in time) component of the response in the same way as described in detail in [14], the third-harmonic light is generated by the oscillating component of the response.

We have offered an intuitive understanding of the ring and axial parts of the TH radiation and their dependence on the focusing geometry. The axial component can be compared to a forced oscillator driven (by the fundamental) at a frequency away from resonance. This provides a simple explanation for the fact that fundamental and TH waveforms propagate together with a nearly fixed phase-shift of π, and that the TH axial intensity tends to follow the intensity of the fundamental. Phase-matching plays a crucial role for appearance of the ring. The distribution of the ring energy in the angle-frequency space reflects both the transverse and longitudinal dimensions of the filament.

Even in the extreme cases when the angle-integrated SC and TH spectra merge completely, the two radiation components remain distinct in the angle-frequency space. Only for long interaction distances (i.e. long filaments) and high pulse energies can SC spectrum grow to such an extent that the TH contribution effectively disappears on its background even in the angle-resolved spectrum.

The fact that in most situations one can clearly identify the origin of the radiation (SC vs.TH generation) based on the far-field spectrum, makes it possible to study how different mechanisms affect the spectral dynamics of the pulse. We have shown, by comparing simulations with and without TH generation included in the model, that TH radiation doesn't change the mechanism that generates the supercontinuum.

ACKNOWLEDGEMENTS This work was supported by the Air Force Office for Scientific Research under grants F49620-03-1-0194, FA9550-04-1-0213, FA9550-04-1-0355, and by the NLWD under grant M67854-06-1-5005.

REFERENCES

1 S. Backus, J. Peatross, Z. Zeek, A. Rundquist, G. Taft, M.M. Murnane, H.C. Kapteyn, Opt. Lett. **21**, 665 (1996)
2 C.W. Siders, N.C. Turner III, M.C. Downer, A. Babine, A. Stepanov, A.M. Sergeev, J. Opt. Soc. Am. B **13**, 330 (1996)
3 A.B. Fedotov, N.I. Koroteev, M.M.T. Loy, X. Xiao, A.M. Zheltikov, Opt. Commun. **133**, 587 (1997)
4 J. Peatross, S. Backus, J. Zhou, M.M. Murnane, H.C. Kapteyn, J. Opt. Soc. Am. B **15**, 186 (1998)
5 G. Marcus, A. Ziegler, Z. Henis, J. Opt. Soc. Am. B **16**, 792 (1999)
6 N. Aközbek, A. Iwasaki, A. Becker, M. Scalora, S.L. Chin, C.M. Bowden, Phys. Rev. Lett. **89**, 143 901 (2002)
7 I. Alexeev, A.C. Ting, D.F. Gordon, E. Briscoe, B. Hafizi, P. Sprangle, Opt. Lett. **30**, 1503 (2005)
8 F. Théberge, N. Aközbek, W. Liu, J.-F. Gravel, S.L. Chin, Opt. Commun. **245**, 399 (2005)
9 F. Théberge, W. Liu, Q. Luo, S.L. Chin, Appl. Phys. B **80**, 221 (2005)
10 F. Théberge, Q. Luo, W. Liu, S.A. Hosseini, M. Sharifi, S.L. Chin, Appl. Phys. Lett. **87**, 081 108 (2005)
11 R.A. Ganeev, M. Suzuki, M. Baba, H. Kuroda, I.A. Kulagin, Appl. Opt. **45**, 748 (2006)
12 L. Bergé, S. Skupin, G. Méjean, J. Kasparian, J. Yu, S. Frey, E. Salmon, J.P. Wolf, Phys. Rev. E **71**, 016 602 (2005)
13 N. Aközbek, A. Becker, M. Scalora, S.L. Chin, C.M. Bowden, Appl. Phys. B **77**, 177 (2003)
14 M. Kolesik, E.M. Wright, J.V. Moloney, Opt. Express **13**, 10729 (2005)
15 M. Kolesik, J.V. Moloney, M. Mlejnek, Phys. Rev. Lett. **89**, 283 902 (2002)
16 M. Kolesik, J.V. Moloney, Phys. Rev. E **70**, 036 604 (2004)
17 E.R. Peck, K. Reeder, J. Opt. Soc. Am. **62**, 958 (1972)
18 M. Mlejnek, E.M. Wright, J.V. Moloney, Opt. Lett. **23**, 382 (1998)
19 W. Liu, S.L. Chin, Opt. Express **13**, 5750 (2005)
20 M. Born, E. Wolf, *Principles of Optics*, 7th edn. (University Press, Cambridge, 1999)
21 J. Muth-Böhm, A. Becker, F.H.M. Faisal, Phys. Rev. Lett. **85**, 2280 (2000)
22 H. Yang, J. Zhang, J. Zhang, L.Z. Zhao, Y.J. Li, H. Teng, Y.T. Li, Z.H. Wang, Z.L. Chen, Z.Y. Wei, J.X. Ma, W. Yu, Z.M. Sheng, Phys. Rev. E **67**, 015 401(R) (2003)
23 M. Kolesik, E.M. Wright, J.V. Moloney, Phys. Rev. Lett. **92**, 253 901 (2004)
24 M. Kolesik, G. Katona, J.V. Moloney, E.M. Wright, Phys. Rev. Lett. **91**, 043 905 (2003)
25 G. Méjean, J. Kasparian, J. Yu, S. Frey, E. Salmon, R. Ackermann, J.P. Wolf, L. Bergé, S. Skupin, Appl. Phys. B **82**, 341 (2006)